Sunlight photoactivity of rice husks-derived biogenic silica

María de Cordoba, Juan Matos, Ricmary Montaña, Po Poon, Silvania Lanfredi, Fabiano Praxedes, Juan Hernández-Garrido, José J Calvino, Elena Rodríguez-Aguado, Enrique Rodríguez-Castellón, et al.

Fernández de Córdoba MC, Matos J, Poon Ps, Lanfredi S, Preaxedes FR, Hernández-Garrido JC, Calvino JJ, Rodríguez-Aguado E, Rodriguez-Castellón E, Ania CO, Sunlight photoactivity of rice husks-derived biogenic silica, Catal. Today 328 (2019) 125-135. 10.1016/j.cattod.2018.12.008

hal-02108640v1

Sunlight photoactivity of rice husks-derived biogenic silica

María C. Fernández de Cordoba[a,b], Juan Matos[a,c]*, Ricmary Montaña[a], Po S. Poon[a], Silvania Lanfredi[d], Fabiano R. Praxedes[d], Juan C. Hernández-Garrido[e], José J. Calvino[e], Elena Rodríguez-Aguado[f], Enrique Rodriguez-Castellón[f], Conchi O. Ania[b,]*

[a] Bioenergy Department, Technological Development Unit, University of Concepcion, Chile.

[b] CEMHTI CNRS (UPR 3079), Univ. Orleans, Orleans, France.

[c] Millenium Nuclei on Catalytic Processes towards Sustainable Chemistry (CSC), Chile.

[d] São Paulo State University (Unesp), Laboratory LaCCeF, Presidente Prudente, Brazil.

[e] Department of Materials Science and Metallurgy Engineering and Inorganic Chemistry, Faculty of Sciences, University of Cadiz, Puerto Real (Cadiz), Spain.

[f] Inorganic Chemistry Department, Faculty of Science, University of Malaga, Spain.

*Corresponding authors. Tel.: +56-412661905. E-mail addresses: jmatoslale@gmail.com, j.matos@udt.cl (J. Matos); conchi.ania@cnrs-orleans.fr (C.O. Ania)

Abstract

Carbon-containing SiO_2-based photocatalysts were prepared by the solvothermal treatment of rice husk as biogenic precursor in the presence and absence of TiO_2 and used for the photocatalytic degradation of rhodamine-B under simulated solar light. Data showed that the prepared catalysts are mainly composed of biogenic silica and displayed mesoporous character with surface areas ranging from 65 to 174 m^2 g^{-1}. The obtained materials showed photocatalytic activity comparable to that of commercial TiO_2-P25 powders for the degradation of rhodamine-B under sunlight. The calcination at 350 ºC improved the photocatalytic activity of the biogenic precursor by three times in the absence of TiO_2. At converse, calcination of sample SiO_2-TiO_2 decreased the photoactivity due to the appearance of non-photoactive $TiSiO_4$ crystalline phases in the catalyst, as inferred by XRD and XPS. A reaction mechanism for rhodamine-B degradation excluding the deethylation pathway has been proposed, based on the evolution of the absorbance spectra of rhodamine-B upon the photocatalytic tests.

Keywords: Biogenic silica; rice husks; photocatalysis; rhodamine B; artificial solar light

1. Introduction

TiO_2 is considered the best semiconductor photocatalyst for the degradation of aromatic molecules in water due to several advantages such as a high photostability under UV irradiation, resistance to strong acid/bases, inertness and relatively low cost [1,2]. However, it has important scale-up limitations such as the high and pH-dependent recombination rate, a low absorption of solar light, and the low to moderate surface area of most commercial TiO_2-based photocatalysts, which limits their application to low effluent volumes and low pollutants concentration [3,4]. It has been extensively reported than most of these limitations can be overcome by using various co-supports such as alumina [5], silica [6,7], and activated carbon [8-10].

Among them, it been reported that the photocatalytic activity of TiO_2 can be enhanced by introducing SiO_2, as the titania–silica (TiO_2–SiO_2) mixed oxides benefit from the photocatalytic activity of titania, and the high mechanical and thermal stability of silica [11-14]. The photocatalytic activity of TiO_2/SiO_2 catalysts, being strongly dependent on many synthetic parameters, may be more or less photoactive than titanium dioxide powders, but they usually display better sedimentability properties, thus enabling the separation of the catalyst after the photocatalytic treatment [11-14]. Furthermore, as the production of silica can be cheaper than that of titania, the costs of the photocatalysts can be significantly reduced.

In this context, biogenic (i.e., natural-resources-based) silica is receiving an increasing attention in different fields covering wastewater treatment [15], biomedicine [16], energy storage in batteries [17] and catalysis [18], due to the availability, low cost and sustainability of these

materials. However, scarce studies have focused on its potentialities in solar photocatalysis due to the low sunlight absorption coefficient of most silica-based materials [19,20].

Keeping this in mind, the main objective of this work was to prepare biogenic silica and silica-TiO_2 hybrid catalysts from an abundant biomass waste, and to evaluate their photocatalytic activity for the degradation of a recalcitrant dye in aqueous medium under artificial solar light. Rice husk, an agro-waste product largely generated around the world has been used as natural source for the fabrication of the silica-based materials, as is contains ca. 15-20% of inorganic (SiO_2) matter. On the other hand, Rhodamine B was chosen as target molecule, as it is a toxic dye, one of the mostly used fluorophores in biotechnology applications [21], and also widely used in cosmetic products. Being a toxic and largely used compound its photocatalytic degradation on various semiconductor-based photocatalysts has been extensively reported [22-26].

2. Experimental

2.1. Synthesis of silica-based materials

Analytical grade titanium (IV) isopropoxide and Rhodamine B (RhB) were purchased from Sigma-Aldrich. Absolute ethanol was purchased from Merck. Rice husk was provided by a Chilean agroindustry company, and it was used as received. The catalysts were prepared by solvothermal treatment of ca. 0.5 g of crushed and sieved rice husks (sample RH) in 9 mL of absolute ethanol in a Teflon-lined autoclave heated at 180 ºC for 16 h. The obtained solid was filtered and washed several times in absolute ethanol and dried under static-air at 100 ºC for 2 h. The resulting catalyst was denoted as RH-Si. A hybrid catalyst was prepared by adding ca. 0.5 g

titanium isopropoxide to the RH suspension in ethanol before the solvothermal treatment (sample RH-Si-Ti). Additionally, a TiO_2 catalyst was synthesized following the solvothermal procedure in the absence of RH (sample TiO_2 synth). Calcination of the catalysts was carried out in a muffle at 350 °C for 2 h under static air; calcined samples were denoted RH-Si-350 and RH-Si-Ti-350. Commercial TiO_2 (P25, Evonik) and amorphous SiO_2 (Sigma-Aldrich) were also used for comparative purposes.

2.2. Characterization of materials

The texture of the materials was characterized by measuring the N_2 adsorption-desorption isotherms at -196 ºC (Micromeritics equipment). The samples were previously outgassed under dynamic vacuum (ca. 10^{-5} Torr) at 200ºC for 17 h. Ultrahigh purity gas (i.e., 99.9992 for N_2) was supplied by Air Products. The isotherms were used to evaluate the specific surface area (BET equation), the total pore volume (evaluated at a relative pressure of 0.99) and the micropore volume from the Dubinin-Radushkevich formulism [27].

The surface pH of the materials was measured as the pH of a suspension of the catalysts in distilled water (ca. 50-5 mg of solids in 20 mL) under stirring at 800 rpm [28]. The pH of the suspension was measured until a constant value (ca. 1-2 h) and plotted as a function of the amount of catalyst in the suspension. The surface pH was considered as the value at the plateau of the representation.

The carbon content in the catalysts was estimated from gravimetric analysis.

Chemical bonds were studied by Fourier transformed infrared spectroscopy (FTIR). The sample was diluted in KBr (ratio of 1:100) and the measurements were carried out in the range of 4000–400 cm^{-1} with a resolution of 4 cm^{-1} for 100 scans (Shimadzu, IR Affinity-1).

X-ray diffractograms on powder samples were obtained using a Shimadzu (model XRD-6000) diffractometer, with Cu-Kα1 radiation (k = 1.54056 Å) provided with a graphite monochromator and operating at 40 kV and a current of 30 mA. Measurements were carried out over an angular range of 5-80° with a scanning step of 0.02° and a fixed counting time of 10 s. Divergence, scattered and receiving radiation slits were 1^o, 1^o and 0.2 mm respectively. From XRD measurements, a Crystallinity Index (CI) was calculated as proposed by Focher and coworkers [29] using the equation (1):

$$\text{Crystallinity index (\%)} = \frac{I_{111} - I_{am}}{I_{111}} \text{x100} \qquad (1)$$

where I_{111} is the maximum intensity value for the scattering angle of silica phase at 2θ of 22º and I_{am} is the minimum intensity value of the amorphous diffraction peak at 17º.

The optical features were evaluated from UV-Vis diffuse reflectance spectroscopy, recorded on a spectrophotometer equipped with an integrating sphere, and using $BaSO_4$ as a reference. Absorbance and reflectance measurements were carried out between 220 and 700 nm and transformed to a magnitude proportional to the extinction coefficient through the Kubelka-Munk function, F(R∞). The energy band gaps (E_g) were estimated from the Tauc representation using a double linear fitting.

The morphology and microstructure of the samples was studied by scanning electron microscopy (SEM) and energy dispersed X-ray (EDX). SEM images were acquired in a (FEG) SEM Nova NanoSEM 450, operated at 24 kV, with integrated EDX system (EDAX TEAM^{TM}) to perform elemental composition analysis on the targeted region of interest.

The surface atomic composition of samples was analysed by X-ray photoelectronic spectroscopy (XPS). XPS measurements were carried on a Physical Electronics spectrometer (PHI Versa Probe II Scanning XPS Microprobe, Physical Electronics, Chanhassen, MN, USA) with monochromatic X-ray Al Kα radiation (100 μm, 100 W, 20 kV, 1486.6 eV) and a dual beam charge neutralizer. The energy scale of the spectrometer was calibrated using Cu $2p_{3/2}$, Ag $3d_{5/2}$ and Au $4f_{7/2}$ photoelectron lines at 932.7, 368.2 and 84.0 eV, respectively. Under a constant pass energy mode at 23.5 eV condition, the Au $4f_{7/2}$ line was recorded with 0.73 eV FWHM at a binding energy (BE) of 84.0 eV. The collected XPS spectra were analyzed using PHI SmartSoft software and processed using MultiPak 9.3 package. The binding energy values were referenced to adventitious carbon C 1*s* signal (284.8 eV). Recorded spectra were always fitted using Gauss–Lorentz curves. Atomic concentration percentages of the characteristic elements of the surfaces were determined considering the corresponding area sensitivity factor for the different measured spectral regions.

2.3. Adsorption studies and photocatalytic tests

Rhodamine-B (RhB) was selected as recalcitrant dye to carry out the adsorption and photocatalytic degradation tests, using UV-visible spectroscopy (554 nm) to follow the extent of the reaction. Initially, kinetics studies were performed to evaluate the adsorption capacity of the catalysts in the dark. For this, solutions of RhB of various initial concentrations ranging from 2 to 20 mg L^{-1} were put in contact with ca. 1 g L^{-1} of catalyst. An equilibration time of 90 min was obtained for all the catalysts; thus this value was used for all the experiments to evaluate the equilibrium adsorption isotherms. Equilibrium experimental isotherms were fitted to both Freundlich and Langmuir models. For the photocatalytic tests, a Pyrex open-to-air photoreactor

was used with 125 mL of solution and 125 mg of catalyst. Commercial silica (SiO_2 comm) and titania (TiO_2-P25) were used for comparison purposes. Irradiation was performed with a solar simulator box equipped with a Xe-lamp emitting the solar spectrum (photon flux ca. 3.2×10^{19} photons m^{-2} s^{-1}). The radiation intensity in the UV region was ca. 20 W m^{-2} measured with a radiant power meter, corresponding to a total radiation intensity of 250 W m^{-2}. The amount of photocatalyst in the suspension was constant (ca. catalyst loading of 1 g L^{-1}) for all the samples. However, for a proper comparison, equivalent amounts of commercial silica or titania matching the composition of the hybrid catalysts were also measured. The initial concentration of RhB in solution in the photocatalytic tests was adjusted based on the dark adsorption assays, to assure the same concentration in solution for all the catalysts (ca. 8.5 mg L^{-1}) when the illumination was applied. All the experiments were performed at least in duplicates, and the accuracy of the experiments was found to be below 2%. Here, average data is presented.

3. Results and discussion

3.1. Characterization of the materials

Figure 1 shows a series of SEM images of the rice husk raw material after crushing and sieving. The typical morphology of the biomass precursor is observed, characterized by an aligned cellular structure. Interestingly, the raw biomass displayed a well-ordered mountain-valleys microstructure (**Fig. 1c**), similar to that commonly reported for cross-linked polymerized hydrogels [30]. **Figure 2** shows the SEM images corresponding to the catalysts prepared by the

solvothermal treatment of the rice husks, so as to investigate the evolution of the morphology and microstructure of the precursor upon the modification.

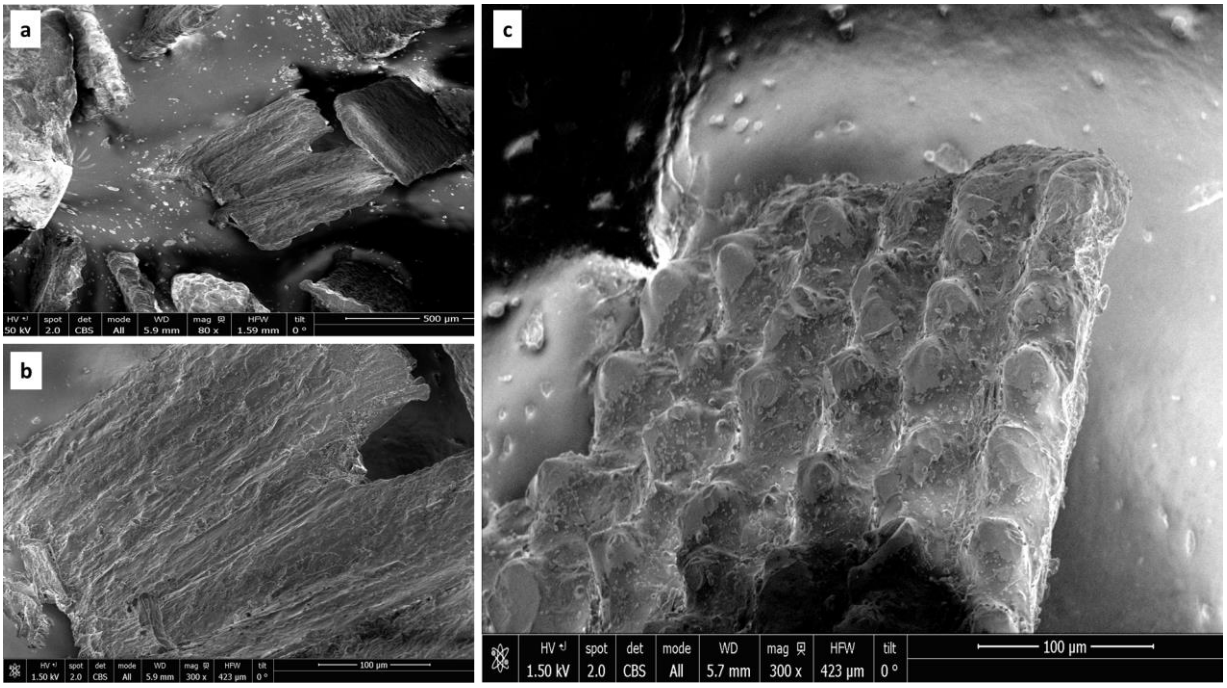

Figure 1. SEM images of the raw rice husk precursor at various magnifications.

After the solvothermal treatment at 180°C (sample RH-Si), the morphology of the rice husks is preserved, with the mountain-valley morphology evolving to a flat surface (**Fig. 2a, 2b**). After calcination at 350°C (sample RH-Si-350), the sample displayed an amorphous morphology (**Fig. 2c**, **2d).** For the case of Ti-containing samples (**Fig. 2e**, **2f),** the mountain-valley morphology of the precursor is preserved after the solvothermal treatment, indicating that the Ti-species do not have a strong influence in the morphology of SiO_2-based material (**Fig. 2e**).

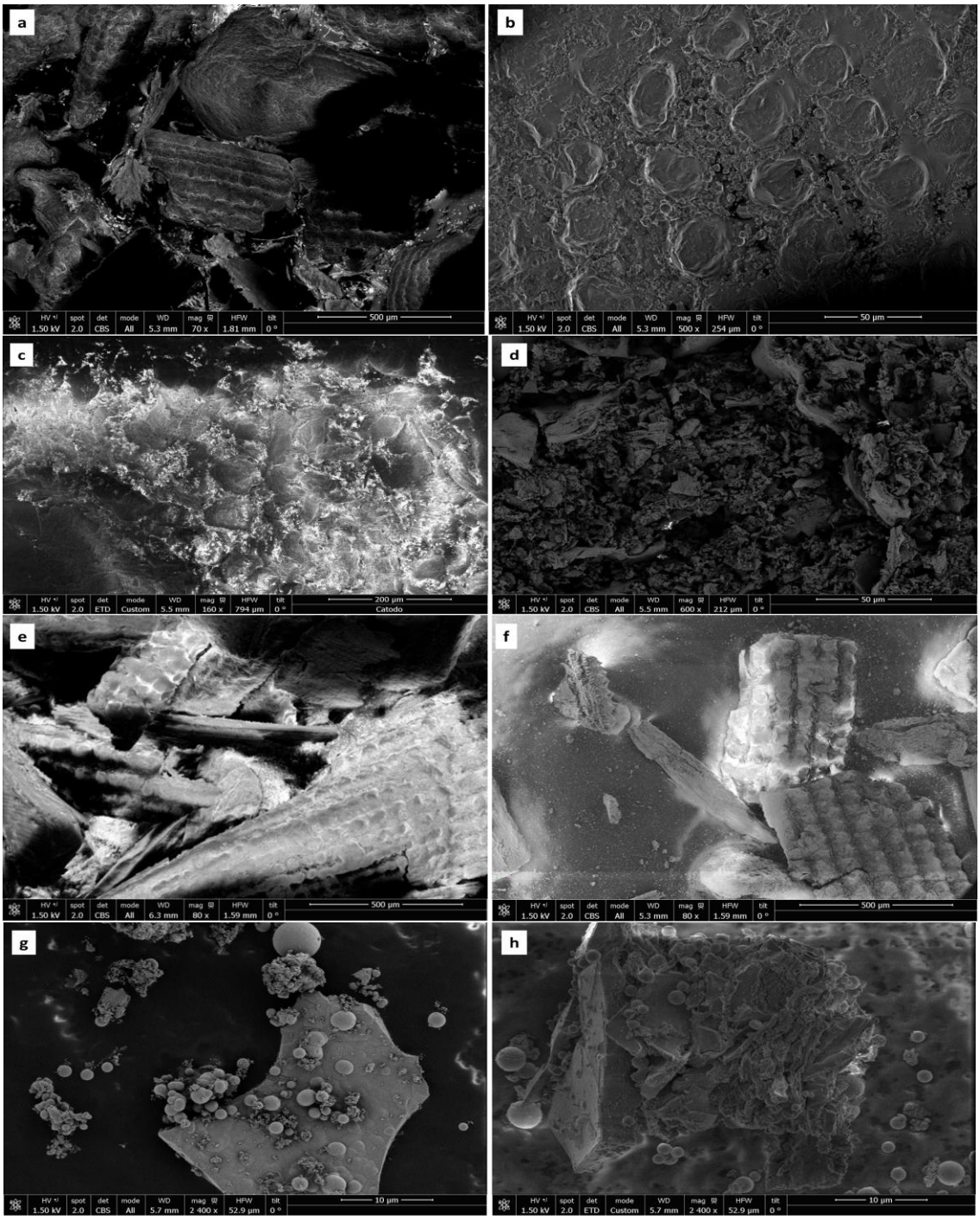

Figure 2. SEM images of the prepared catalysts. (a-b): RH-Si; (c-d): RH-Si-350; (e-f): RH-Si-Ti; (g-h): RH-Si-Ti-350.

A small cracking of the husks particles is also observed during the solvothermal treatment (**Fig. 2f**); for the Ti-containing sample after calcination (RH-Si-Ti-350) spherical (globular) particles are clearly observed (**Fig. 2g**, **2h**), likely suggesting some particles coalescence during calcination.

For a better understanding of the interaction between the biogenic-silica matrix and the Ti-containing particles, a SEM-EDX analysis was performed to sample RH-Si-Ti-350 (**Fig. 3**) in different regions (marked as 1 and 2). As seen, the spherical particles are embedded within the planar surface of the matrix (**Fig. 3a, 3b**). The EDX spectrum of the different regions (**Fig. 3c**, **3d, 3g, 3h)** shows the different composition: rich in Si and rich in Ti atoms. For instance, the planar particles in **Figures 3b** and **3e (region 1)** are mainly composed by Si atoms (ca. 19.6 and 3.3 at.% for Si, and Ti, respectively), while the spherical ones (region 2) are predominantly composed by Ti atoms (ca. 2.4 and 22.6 at.% for Si and Ti, respectively). In both regions, the almost similar and high oxygen content (ca. 77 and 75 at.%) is consistent with the presence of mixtures of SiO_2 and TiO_2. Furthermore, the high Si composition in region 2 suggests the existence of a more complex crystalline phase such a $TiSiO_4$ (see discussion below).

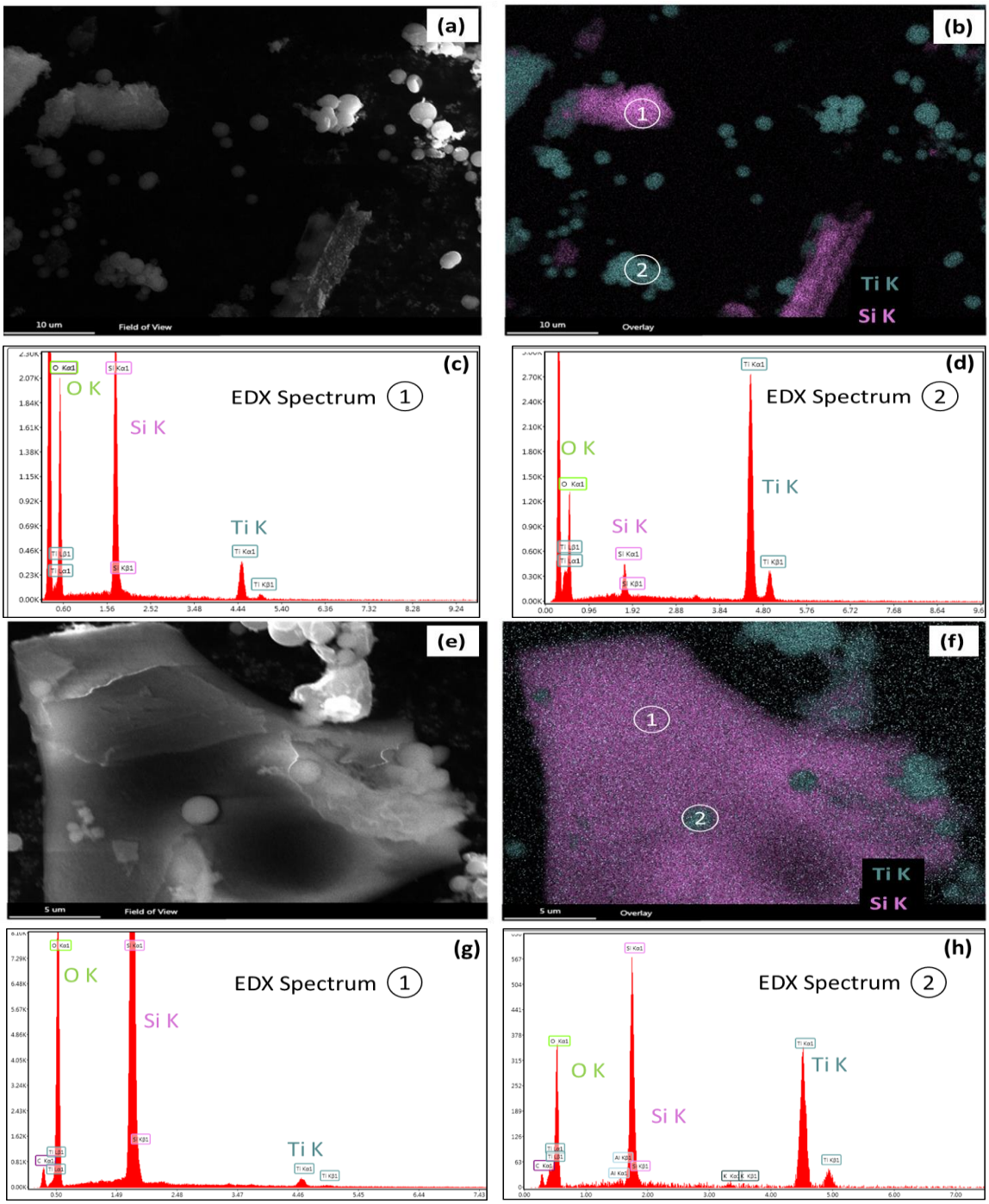

Figure 3. SEM-EDX analysis of sample RH-Si-Ti-350. (a-e): SEM images; (b-f): SEM images showing the analyzed regions; (c-d, g-h): EDX spectra.

The chemical composition of the catalysts was further studied by XPS. **Figure 4** shows the C 1*s* core level spectra of all four samples, while data corresponding to the raw rice husks is show in **Figure S1** in the Supplementary Material File. For all the samples, the C 1s core level spectra were deconvoluted to three main contributions: the intense peak at 284.9 eV was assigned to graphitic carbon in sp^2 configurations; the peak at 286.5 eV to C-O, C-H bonds (phenolic, alkoxy, ether), and the contribution featuring at 288.2 eV was assigned to O-C=O bond (carboxylic, ester groups). These functional groups are generally found in lignocellulosic materials [31] such as cellulose and biomass wastes.

Interestingly, important modifications were obtained upon the solvothermal and calcination treatments. RH-Si sample showed a marked contribution of the signal at 286.5 eV (**Fig. 4a**) assigned to carbonyl groups. This is in agreement with previous works from the literature reporting the large proportion of carbonyl groups for nanostructured materials prepared by solvothermal synthesis of biomass [32, 33]. The effect was not so pronounced for sample RH-Si-Ti sample (**Fig. 4c**), suggesting that the incorporation of Ti avoids the formation of these groups and/or promotes its decomposition. The contribution of both carbonyls and carboxylic groups clearly decreases after calcination (**Fig. 4b, 4d**).

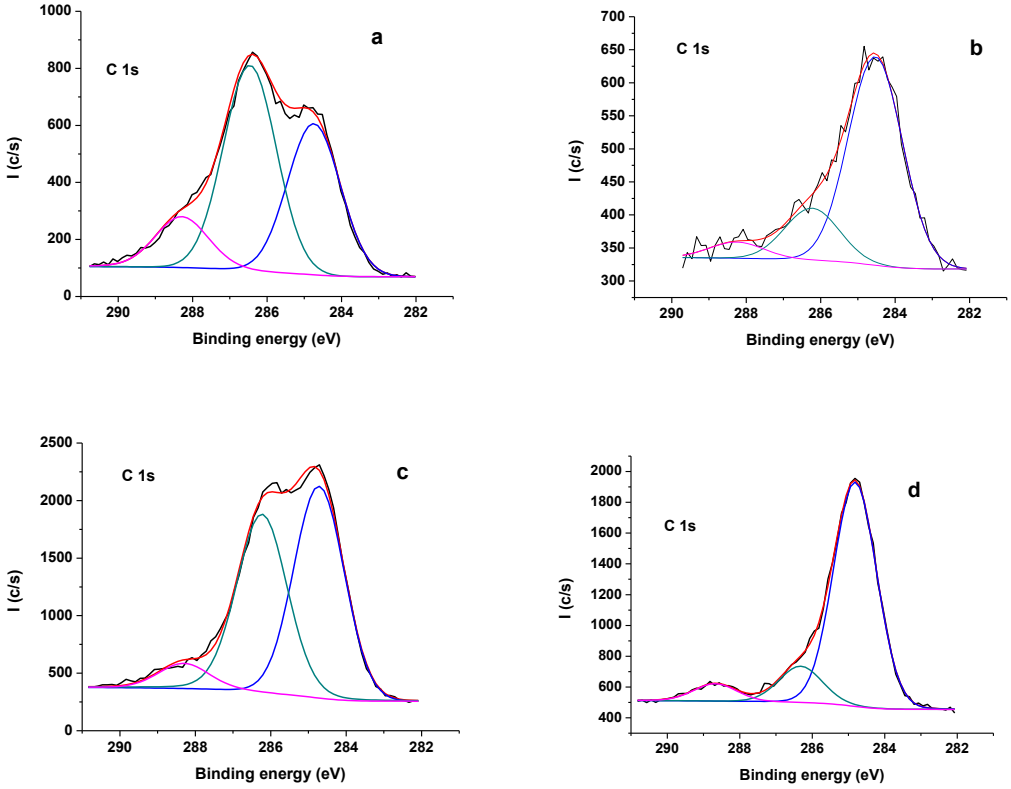

Figure 4. C 1*s* core level spectra for the synthesized catalysts: (a): RH-Si; (b): RH-Si-350; (c): RH-Si-Ti; (d): RH-Si-Ti-350.

Table 1 shows a summary of the atomic concentration of the elements detected by XPS for the rice husks and the synthesized catalysts. Besides the expected elements such as C, N, O, Si and Ti, other elements such as N, Mg, and K were detected in some samples at very low atomic concentrations. Thus, no significant influence on the adsorption or the photocatalytic activity would be expected. After calcination, a remarkable decrease in the amount of carbon was observed for the samples regardless the presence of Ti. This is in agreement with the increase in

oxygen. The effect was more pronounced for the non Ti-containing samples, which could be due to a higher interaction between carbon groups and Ti atoms.

Table 1. Summary of atomic concentration (at. %) of the elements detected by XPS analysis.

Sample	C	N	O	Si	Ti	Mg	K
RH	65.13	1.87	28.51	4.48	nd	nd	nd
RH-Si	51.63	1.78	40.25	6.34	nd	nd	nd
RH-Si-350	7.39	0.77	63.80	26.60	nd	0.83	0.62
RH-Si-Ti	46.19	nd	41.95	0.56	11.07	nd	0.23
RH-Si-Ti-350	17.84	nd	57.92	7.48	16.38	nd	0.38

[a] nd: not detected.

The increase in Si after calcination is also remarkable, with values 4 and 13 times higher for RH-Si-350 and RH-Si-Ti-350, respectively, than their corresponding non-calcined counterparts. The low Si amount of sample RH-Si-Ti should be pointed out; this suggests the presence of silica particles embedded in the matrix, that would diffuse to the surface upon calcination. In addition, the ratio Ti/Si is *ca.* 19.8 for RH-Si-Ti and *ca.* 2.2 for RH-Si-Ti-350, suggesting a strong interaction between Si and Ti atoms during the calcination.

This was confirmed by the analysis of the O 1*s* core level spectra of the samples (**Fig. 5)**. As seen, the spectra of samples RH-Si and RH-Si-350 (**Fig. 5a**, **5b**) are practically similar, with a main peak at *ca.* 533.0 eV assigned to O-Si bonding in a SiO_2 structure [34]. In this case, calcination of sample (RH-Si-350) caused an increase in the intensity of the spectrum, indicating a better annealing of SiO_2. In the presence of Ti, the O 1*s* core level spectra were deconvoluted to

3-4 contributions (**Fig. 5, 5d**), suggesting different interactions between O, Si and Ti atoms. For the sample RH-Si-Ti, contributions at 531.7 and 530.0 eV were observed, attributed to O-Ti bonding in a complex framework $SiTiO_4$, and to O-Ti bonding in the TiO_2 framework, respectively. For the sample RH-Si-Ti-350, an additional peak at 534.0 eV was also attributed to O-Si bonding in a complex framework $SiTiO_4$.

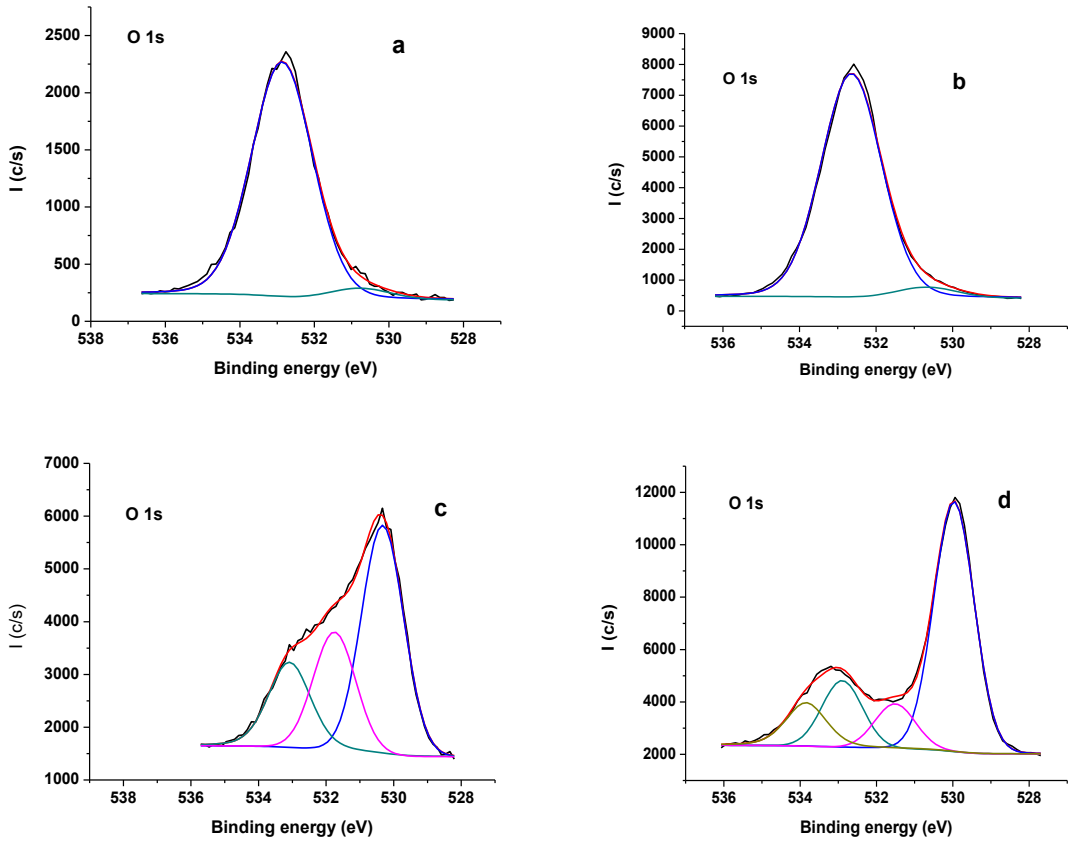

Figure 5. O 1*s* core level spectra of the synthesized catalysts: (a): RH-Si; (b): RH-Si-350; (c): RH-Si-Ti; (d): RH-Si-Ti-350.

In sum, calcination of RH-Si-Ti sample yields a thermally stable material with nanocrystalline domains of various inorganic oxide frameworks. This complex structure and the binding energy assignments for the O 1s region of XPS spectra can be figure out by a super-cell $Si_3Ti_3O_{12}$ showed in the **Fig. S2** (supplementary material). The formation of this ordered SiO_2/TiO_2 complex structure suggest a kind of assembly mechanism similar than for the case of inorganic oxides/blocks copolymer assemblies reported by Yang and coworkers [35].

Figure 6a shows the N_2 adsorption-desorption isotherms at -196 ºC of the synthesized catalysts and the rice husk precursor (RH) before the solvothermal treatment. A summary of textural properties and physicochemical parameters of the samples is compiled in **Table 2.**

All the catalysts displayed a moderate porosity dominated by mesopores, with surface areas ranging from 65 to 174 $m^2\ g^{-1}$ (**Table 1**). The calcination treatment increased the surface area of the catalysts, with sample RH-Si-350 showing a BET surface area one order magnitude higher than that of RH-Si. In the presence of titania, the effect of the calcination on the surface area was less pronounced, accounting for an increase of ca. 2.7. The samples also displayed different carbon content, following the order: RH-Si-Ti-350 < RH-Si-350 < RH-Si-Ti ~ RH-Si. The carbon content was quite similar for the non-calcined samples regardless the presence of titania, suggesting that TiO_2 does not modify the decomposition of the RH in the solvothermal process. The slight difference in the carbon content between RH-Si-Ti-350 and RH-Si-350 could be attributed to a more acidic pH in the Ti-containing sample, being responsible of a higher consumption of carbon atoms in the calcination. After calcination the surface pH of RH-Si became more basic, likely due to the elimination of functional groups of acidic nature

[32] -typically observed after the solvothermal synthesis of biomass- and/or to the formation of metallic silicates.

Table 2. Selected textural, chemical and structural properties of the studied catalysts.

Sample	S_{BET} [a] ($m^2 g^{-1}$)	V_{total} [b] ($cm^3 g^{-1}$)	Wo_{DR} [c] ($cm^3 g^{-1}$)	Carbon [d] (wt.%)	pH [e]	CI [f] (%)	D [g] (nm)
RH	5	0.01	0.00	40.8	--	50.6	1.47 (SiO_2 111)
RH-Si	10	0.02	0.01	18.5	6.7	50.3	1.58 (SiO_2 111)
RH-Si-350	101	0.13	0.03	5.0	8.2	--	0.77 (SiO_2 111)
SiO_2 comm	250	0.40	--	--	6.5	--	--
RH-Si-Ti	65	0.07	0.02	17.2	6.0	46.2	2.11 (SiO_2 111)
RH-Si-Ti-350	174	0.20	0.05	3.0	5.9	--	4.79 (TiO_2 101)
TiO_2-P25	45	0.08	0.00	< 0.1	6.4	--	--
TiO_2-synth	--	--	--	--	5.9	--	--

[a] BET specific surface area. [b] Total pore volume evaluated at at P/Po ≅ 0.99. [c] Micropore volume evaluated using the Dubinin-Raduskevich method. [d] Carbon content obtained from gravimetric analysis. [e] Surface pH. [f] Crystallinity index defined by eq. (1). [g] Average crystallite size obtained by Scherrer's equation.

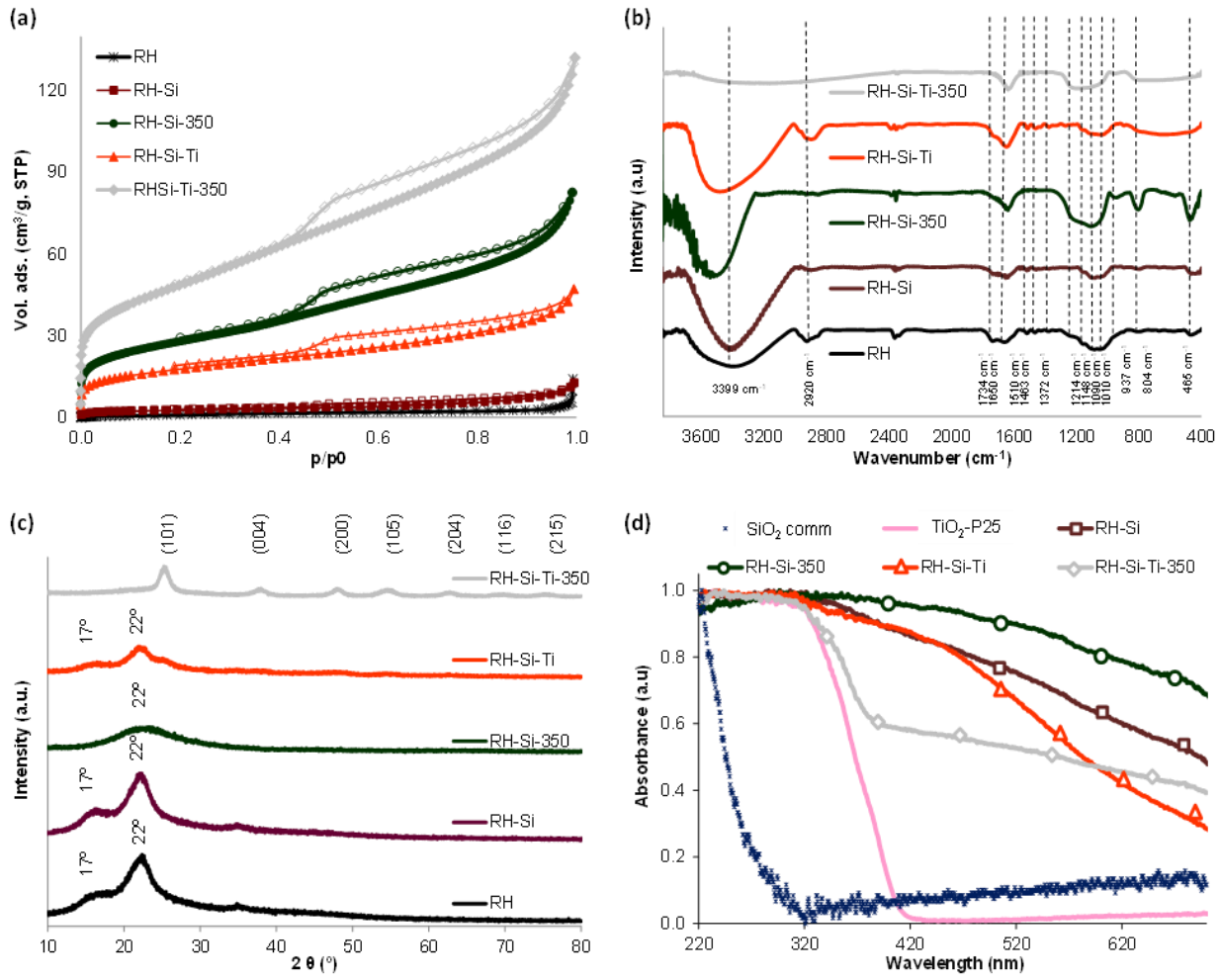

Figure 6. Characterization of the prepared catalysts: (a) N_2 adsorption-desorption isotherms at -196 ºC; (b) FTIR spectra; (c) XRD patterns; (d) light absorption features.

Figure 6b shows the FTIR spectra for the studied samples; a summary of the band positions and characteristics observed in the FTIR spectra are listed in **Table S1** in the Supplementary File. The absorption bands in the rice husks spectra are attributed to physically adsorbed water, functional groups of cellulose, hemicellulose and lignin, as well as the inorganic components in their

composition [36]. Samples RH, RH-Si and RH-Si-350 present an absorption band at 804 cm^{-1} attributed to the symmetric vibrations of the Si–O bonds in the silicon-oxygen tetrahedrons (SiO_4) [37,38]; the bands at around 465 cm^{-1} are assigned to Si-O-Si bending vibrations [39]. The latter band was not clearly observed in the Ti-containing samples. The variations in the intensity of the peak at 1650 cm^{-1} -attributed to δ-H_2O deformation and the presence of C=C bonds in organic components- are remarkable, with samples RH-Si and RH-Si-350 showing a lower intensity than RH-Si-Ti and RH-Si-Ti-350. This is indicative of changes in the polarity of the samples after the incorporation of Ti [39], in agreement with their more basic (hydrophobic) character as inferred from the surface pH values (**Table 2**).

Figure 6c shows the XRD patterns of the studied samples; RH and RH-Si showed a diffraction line at 22^o related to amorphous SiO_2, and another peak at 17^o associated with the remnant carbon matrix. RH-Si-350 sample showed a remarkable decrease in the crystallinity, represented by the broadening of the peak at 22^o. In the case of RH-Si-Ti, the diffraction bands related to the crystalline phase anatase of TiO_2 were observed, with an increase in the crystallinity after the calcination.

For RH-Si-Ti-350, the phase associated to SiO_2 was no longer observed, suggesting that the silica phase is embedded within the crystalline framework of TiO_2 [40]. This phenomenon would be associated with a redispersion of SiO_2 nanoparticles, since a similar behavior (i.e., decrease in the average crystallite size) was obtained after calcination of RH-Si (**Table 2**). Indeed, it seems reasonable that the particles of SiO_2 located nearby the TiO_2 ones would promote the formation of the $TiSiO_4$ phase observed by SEM, XPS and FTIR data as discussed above. The XRD pattern

of the titanium silicate would overlap with that TiO_2 anatase phase (JCPDS card # 21-1272), the only phase detected in RH-Si-Ti-350.

The different crystallinity of the samples was quantified using the Crystallinity index (CI), calculated as the ratio between the intensity at 22^o and that at 17^o of silica bands, as proposed by Focher et al [29]. The obtained values (**Table 2**) indicate no modification of this parameter for RH and RH-Si, and a decrease for RH-Si-Ti, suggesting that the change of crystallinity is dependent on the presence of titanium. Data also showed that sample RH-Si-350 is an amorphous material, while for RH-Si-Ti-350, the CI cannot be evaluated since the silica bands were no longer observed.

Figure 6d shows the UV-visible absorbance spectra of the prepared catalysts along with commercial TiO_2 and SiO_2. The spectrum of TiO_2-P25 presented the characteristic absorption sharp edge of the anatase form of TiO_2 (predominant phase) in the UV region rising above 400 nm, rendering a band gap value of 3.09 eV, in agreement with the values reported for this material [1-4]. A remarkably high intensity in the absorbance spectra was observed in the visible range for all the biogenic silica-based samples compared to TiO_2-P25 and SiO_2, which absorbance were negligible in the visible range. This can be attributed to the carbon content of the samples. After calcination, RH-Si-350 absorbed more photons in the visible range than RH-Si**.** This could be associated to the larger surface area and lower average crystallite size of this sample, since both parameters have been associated with low light scattering features [41,42]. RH-Si-Ti-350 showed a different trend with a UV-vis spectrum with two-components of absorbance; the one in the UV region corresponds to the absorption cut-off of TiO_2, with a slight red-shift compared to TiO_2-P25. The second region in the visible light is associated to the absorption of the carbon

phase itself. The corresponding energy band gap (E_g) value of and RH-Si-Ti-350 was 3.4 eV agrees with the value reported in the literature for $TiSiO_4$ materials based [43].

3.2. Adsorption studies

The equilibrium adsorption isotherms of RhB on all the studied catalysts are shown in **Figure 7.** Previous kinetics studies showed that a 90 min of contact time was required for all the catalysts to attain the equilibrium (**Fig. S3**). The main adsorption parameters obtained from fitting the experimental data to Langmuir and Freundlich models are summarized in **Table 3**.

With the exception of sample RH-Si, data plotted in **Figure 7** showed a good fitting to Freundlich model, with regression coefficients higher than 0.99 (**Table 3**). Fitting of experimental data to Langmuir model (**Fig. S4**) was not so good, with regression coefficients lower than 0.97 in most of cases. Given the better fitting and accuracy of Freundlich model to describe the experimental data, only the adsorption parameters derived from this model will be further discussed (Table 3). As seen in **Figure 7**, the samples displayed quite different uptakes of the dye, with the highest uptake for RH-Si-350, about 15 times higher than that of RH-Si (the least adsorbing sample). This could be attributed to either the higher surface area of the former, or the increase in the surface pH upon calcination (**Table 2**).

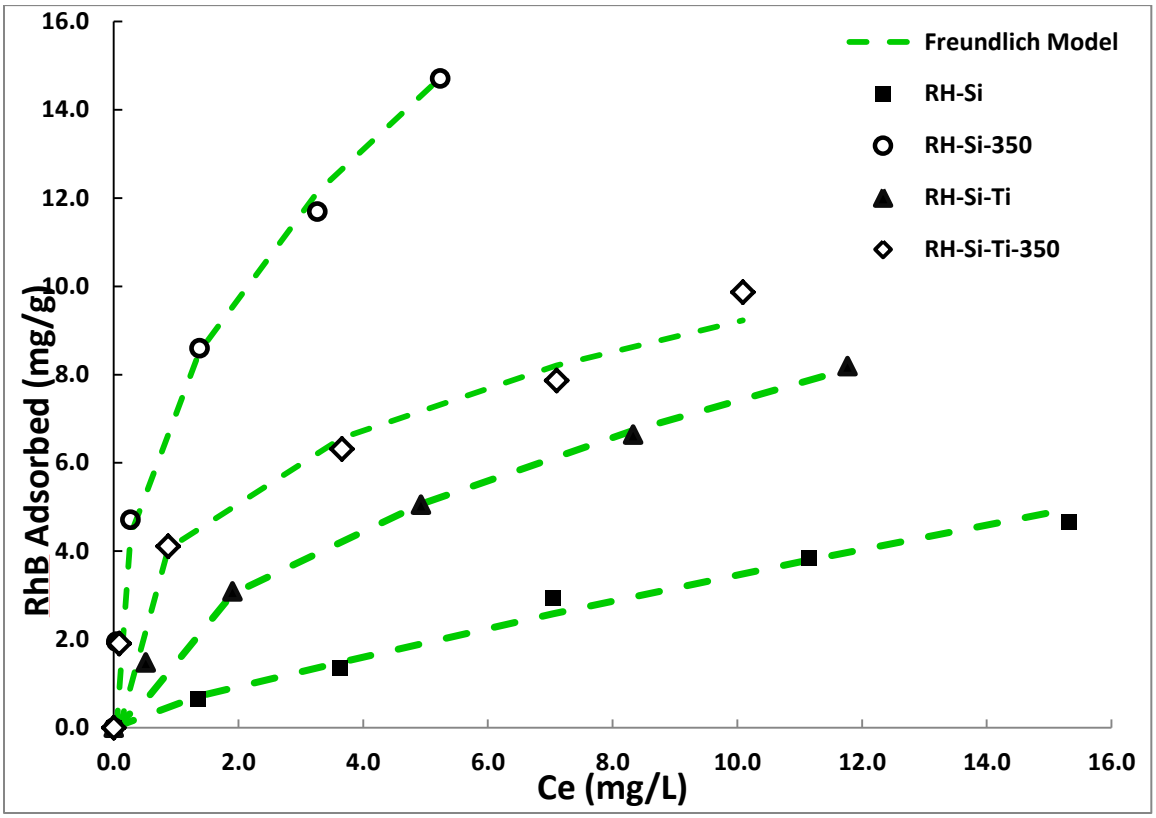

Figure 7. Adsorption isotherms of RhB on the synthesized SiO_2-based catalysts. Symbols account for experimental data; dashed lines to the fitting with the Freundlich model.

No direct correlation between the RhB adsorption and the surface area was found for the Ti-containing samples, indicating the role of the specific interactions between RhB and the surface of the catalysts on the adsorption capacity. Despite the surface area of RH-Si-Ti-350 is higher than that of RH-Si-350, the adsorption capacity of the latter was clearly higher (**Table 3**), suggesting that RhB is adsorbed on the basic sample via interactions between the electron-donor hydroxyl groups in the surface of SiO_2 with the cationic species formed in the diethylamino group in the zwitterion (RhB is a zwitterionic cationic dye, as can be seen from **Figure S5** in the

supplementary material, with a pKa of 3.1 units, being the zwitterion form predominant under our experimental conditions). A similar adsorption mode has been suggested by Chen and coworkers [44] on a negatively charged SiO_2-TiO_2 composite. The higher K_F in RH-Si-350 indicates that the adsorption is favored in basic conditions, where the zwitterionic form of the dye is predominant in solution. In contrast, RhB uptake in the TiO_2-containing samples was practically the same after calcination, despite their differences in surface area and pH (**Table 2**). Freundlich heterogeneity parameter is higher than unity for all the samples, indicating a high surface heterogeneity. The effect is more pronounced after calcination, likely due to a higher exposition of electron-donor groups from biogenic silica and to the increase in surface area [45].

Table 3. Adsorption parameters for RhB obtained from fitting the experimental equilibrium adsorption data to the Langmuir and Freundlich model.

Sample	K_L [a] (L mg^{-1})	q_{max} [b] (mg g^{-1})	R_L^2 [c]	K_F [b] (mg g^{-1})	n_F [c]	R_F^2 [d]
RH-Si	0.07	9.2	0.992	0.5	1.2	0.968
RH-Si-350	1.43	15.7	0.967	7.5	2.4	0.997
RH-Si-Ti	0.23	10.5	0.958	2.1	1.9	0.999
RH-Si-Ti-350	0.78	10.2	0.955	4.3	3.0	0.995

[a] Langmuir adsorption constant; [b] maximum adsorption capacity obtained from Langmuir model; [c] linear regression coefficient for fitting to Langmuir model; [d] Freundlich adsorption constant; [e] Freundlich heterogeneity parameter; [f] linear regression coefficient for fitting to Freundlich model.

3.3. Photocatalytic tests

Figure 8 shows the photocatalytic degradation of RhB on the different photocatalysts, compared to the photolysis of the dye under simulated solar light. The performance of commercial SiO_2 and TiO_2 (P25 and TiO_2-synth) has also been included. **Table 4** compiles the first-order apparent rate-constants (k_{app}) obtained from the fitting of the photodegradation kinetic data after 180 min. Above 180 min the response of the kinetic data was not linear, suggesting the presence of additional reactions (degradation or accumulation of intermediates). The apparent rate-constant was selected to compare the photocatalytic activity of the different materials [46].

Table 4. Kinetic parameters for the RhB photodegradation.

Sample	**Catalyst Loading** **(g L^{-1})**	**n_{ads}** [e] **(μmol)**	**k_{app}** [f] **(x 10^{-3}) (min^{-1})**
SiO_2 comm	0.19	0.23	0.2
TiO_2-P25	0.13	0.37	5.5
TiO_2-synth	0.13	0.11	0.4
RH-Si	1.0	0.75	1.1
RH-Si-350	1.0	3.33	3.4
RH-Si-Ti	1.0	2.96	4.1
RH-Si-Ti-350	1.0	2.40	0.5

[e] RhB adsorbed after 90 min in dark conditions; [f] First-order apparent rate-constant evaluated in the range 0-180 min irradiation time.

The conversion of RhB for the non-containing TiO_2 catalysts **(Figure 8a**) was higher than that of the photolytic reaction. The performance of RH-Si (ca. 25 % RhB conversion) was enhanced after calcination (sample RH-Si-350) with ca. 60 % of conversion after 5 h. The kinetics of the

reaction was also enhanced after the calcination, as seen in the k_{app} value of RH-Si-350 (**Table 3**). This high photocatalytic activity for RH-Si-350 can be attributed to the adequate surface area (**Table 2**), of the material that is responsible for a higher uptake (**Table 3**), and/or the presence of a small but not negligible carbon phase remnant after calcination. Interestingly, the conversion of RhB with the commercial silica powders for a similar catalyst loading was almost negligible.

The incorporation of TiO_2 in the silica-based catalysts improved the photodegradation of the dye (**Fig. 8b**) compared to RH-Si, although different trends were observed for the calcined samples. The conversion of RhB over RH-Si-Ti was ca. 70 %, comparable to that obtained for the commercial benchmark TiO_2-P25, and with a kinetic constant also close to that of the latter. On the contrary, the photocatalytic activity of RH-Si-Ti-350 was quite poor, in terms of RhB conversion (ca. 10 % after 5 h of irradiation) and kinetic constant. This contrasts with the optical features of this sample (**Fig. 6d**), that presented an absorbance profile similar to that of TiO_2, with a cut-off at around 400 nm. This result suggests that the titanium silicate crystalline phase formed during calcination (**Fig. 6b** and **6c,** respectively) is most likely non-photoactive for the degradation of the dye. The decreased photocatalytic activity of RH-Si-Ti-350 (compared to RH-Si-Ti) does not follow the trend of the surface pH, adsorption uptake or porosity. We also attribute this fact to the formation of non-photoactive titanium silicates. Indeed, according to literature [43] different $TiSiO_4$ structures can be commonly found in ABO_4 oxides (e.g., $CrVO_4$-type, zircon, and scheelite) and SiO_2-TiO_2 composites. This polymorph is comprised of regular edge-sharing octahedra of TiO_6 [43] where the silicon atoms occupy the tetrahedral sites constructed by cubic-packed oxygen atom arrays. Thus, the poor photocatalytic activity of sample RH-Si-Ti-350 could be explained by the lack of coordination sites for the adsorption of hydroxyl

moieties and oxygen; this would inhibit the capability of the catalyst to generate oxygen-radical species (i.e., hydroxyl or superoxide radicals) in the compact arrangements of Ti and Si atoms.

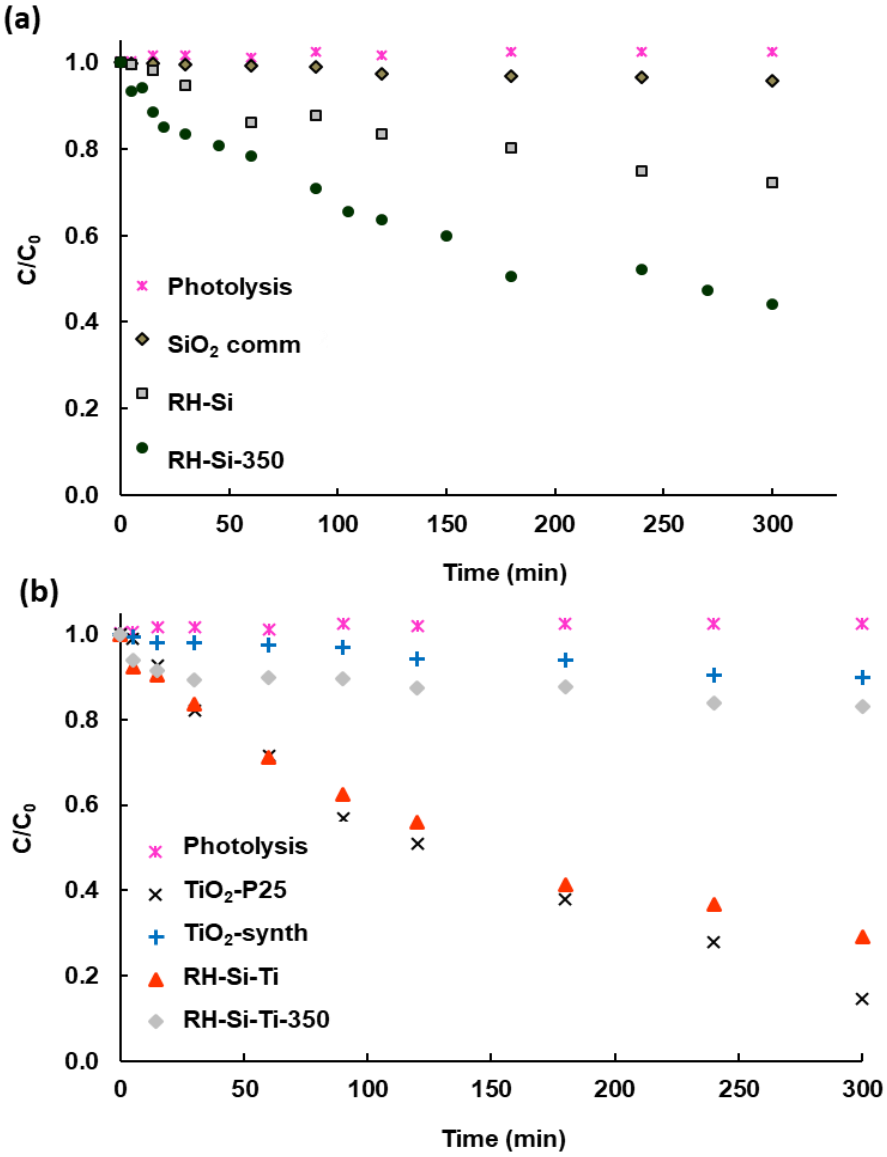

Figure 8. RhB photocatalytic degradation in (a) SiO_2-based and (b): Ti-containing photocatalysts. Data corresponding to the photolytic reaction and the performance of commercial SiO_2 and TiO_2 catalysts is also included for comparison.

It should be noted that the experiments using TiO_2-P25 were performed with an equivalent amount of TiO_2 than that of the hybrid catalysts (ca. 0.134 g L^{-1}). Thus, in terms of kinetic constant (k_{app}), TiO_2-P25 is only 1.3 times more active than herein synthesized materials.

It is also important to correlate the photocatalytic results with the adsorption parameters obtained from Freundlich model (**Table 3**). The higher Freundlich adsorption constant (K_F) of RH-Si-350 points out a high affinity towards the retention of RhB. Then, the superior photoactivity of RH-Si-350 compared to RH-Si (as discussed below) can be attributed to the increased uptake. Furthermore, RhB is a zwitterionic cationic dye with a pK_a of 3.1 units, being predominant the zwitterionic form under our experimental conditions. The high uptake of sample RH-Si-350 indicates that the adsorption is favored in basic conditions, where the zwitterionic form of the dye is predominant in solution. In contrast, RhB uptake in the TiO_2-containing samples was practically the same after calcination, despite their differences in surface area and pH (**Table 2**).

3.4. Mechanism for RhB photodegradation

Considering all the above, we propose a mechanism for the photodegradation of RhB under simulated solar light on the silica-derived catalysts. Rhodamine B has a permanent positive charge (diethylamino group) and a negative charge depending on the ionization state of the carboxylic group for which adsorption is governed by the electrostatic interactions between the surface of the catalysts and the charges in RhB. On negative surfaces RhB is adsorbed by the diethylamino group (positively charged), while for positively charged surfaces the preferred

adsorption mode is through the carboxylic moiety. Under our experimental conditions, RhB is in its zwitterionic form in solution (structure **C** in **Fig. S5)**, while the catalysts are neutral (ca. RH-Si, RH-Si-Ti and RH-Si-Ti-350) or negatively charged (ca. RH-Si-350). Based on the adsorption studies, the uptake is favored in RH-Si-350 (negatively charged according to its surface pH (**Table 2**). Thus, the preferred adsorption mode is through the diethylamino group. This is important since the interactions between the catalyst and the pollutant define the possible photocatalytic degradation pathway.

In the case of RhB, two photodegradation mechanisms have been reported [25,44,47-49], either through successive deethylation steps [25,44,47], or by direct chromophore cleavage [47-49] followed by consecutive oxidations of the aromatic rings. When RhB is adsorbed through the carboxylic moiety in acidic photocatalysts (not the case of the herein studied materials) or at acidic solution pH, the dominant photodegradation mechanism is the deethylation route [25,44,47]. The deethylation route shows a characteristic hypsochromic shift in the UV-vis spectra of the solution, due to the formation of the intermediates (ca. 15-60 nm shift for each deethylation step) [25,44,47]. We did not observe any shift in the UV-visible spectra as a function of the irradiation time for any of the synthesized silica-based photocatalysts (**Fig. 9)** nor for TiO_2-P25 (**Fig. S6).** Furthermore, most performing catalysts showed a basic surface pH. All this points out that the degradation of RhB would proceed through the oxidation of the aromatic ring.

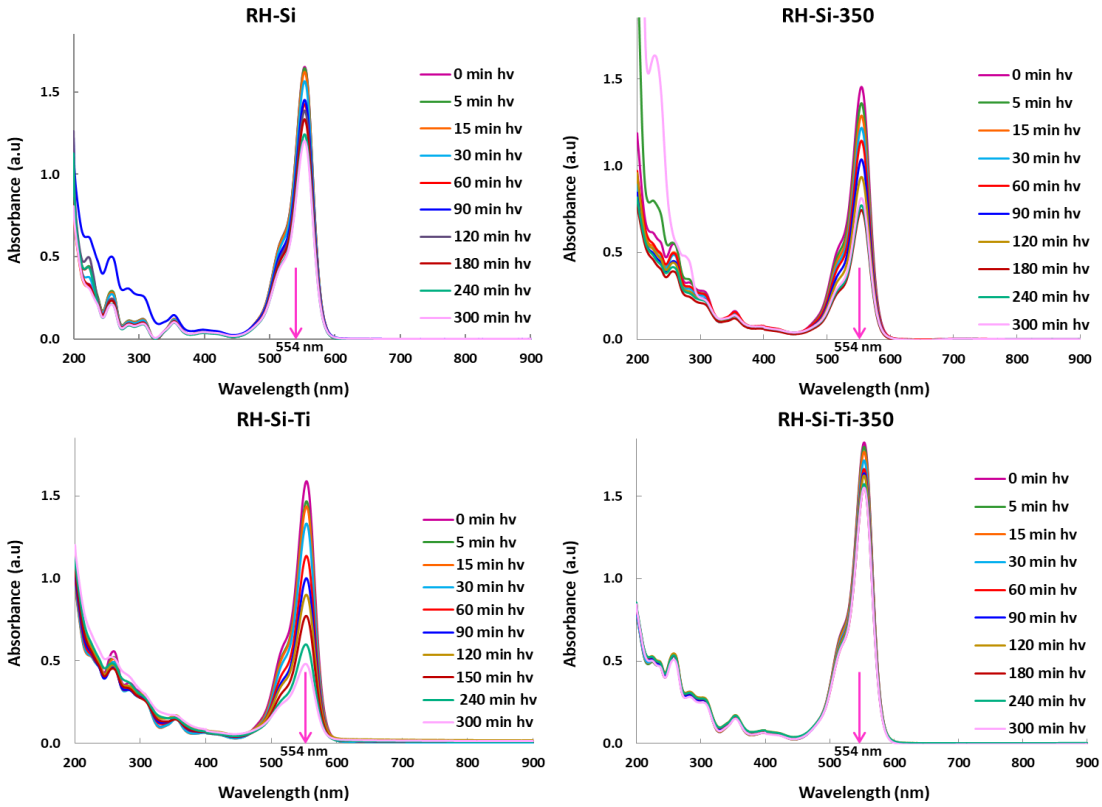

Figure 9. Changes in the absorbance of the UV-visible spectra of the solution as a function of the reaction time for the different biogenic SiO2-based photocatalysts.

On the other hand and given the low degradation yield for the non-catalyzed reaction, the oxidation of RhB is most likely promoted by reactive oxygen species (ROS) formed upon irradiation of the catalysts, as widely reported in the literature for other photocatalytic materials [25,50-54] such as TiO_2 [3,4], $Pb_3Nb_4O_{13}/SiO_2$ [25], Bi-based nanomaterials [47,49-54] and even TiO_2-SiO_2 composites [44].

Considering all this, the most plausible mechanism for the photodegradation of RhB using biogenic silica-based photocatalysts under simulated solar light would consist on the ring-

cleavage of the dye induced by the reaction with ROS (**Figure S7).** This would lead to the formation of hydroxylated intermediates (structure V in **Fig. S7**) upon the photooxidation of two-similar *ortho* positions of one diethylamino group. The degradation of smaller aromatic fragments of RhB formed from the hydroxylation (such as hydroquinone/benzoquinone) can also be inferred from the decrease in the UV region of the spectra (**Fig. 9**).

Finally, it should also be mentioned that the prepared catalysts were well dispersed in the solutions, and allowed an easy and efficient separation of liquid and solid phases during the experiments (compared to TiO_2 nanopowders used as benchmark catalyst). This is most important for photocatalytic degradation purposes where phase separation/filtration steps are involved and it could be related to the adequate surface pH of the catalysts (from almost neutral to a slightly, **Table 2**), Further studies on sedimentability should be carried out to confirm and quantify this behavior.

4. Conclusions

We have prepared hybrid silica-titania-carbon catalysts from the solvothermal treatment of a biomass waste (i.e., rice husks) as biogenic precursor. The prepared materials were used as photocatalysts for the degradation of a recalcitrant dye under solar irradiation. The catalysts are mainly composed of biogenic silica and carbon, depending on the final synthesis step. Indeed, the calcination at 350 ºC of the silica-based catalyst improved its photocatalytic activity of the by three times; at converse, calcination of the silica-titania material rendered a material with lower photocatalytic activity, due to the formation of a non-photoactive crystalline phase (e.g. $TiSiO_4$).

Data also showed that the adsorption mode of rhodamine B defines the photodegradation pathway favoring the degradation through the chromophore cleavage, excluding the deethylation pathway. Furthermore, some of the prepared photocatalyst showed catalytic activity comparable to that of commercial TiO_2-P25 powders for the degradation of a recalcitrant dye under simulated solar light. We believe that the present results open new perspectives for the use of low-cost biogenic-derived materials as low-cost precursors for the synthesis of materials with a large potential as photocatalysts for environmental remediation.

Acknowledgements

Matos and Ania thank the financial support of the Franco-Chilean network BIOCval2E (REDES-170004 project). Matos also thanks the Funding from CONICYT PIA/APOYO CCTE AFB170007, and from Millennium Science Initiative of the Ministry of Economy, Development and Tourism, in Chile (grant Nuclei on Catalytic Processes towards Sustainable Chemistry). Calvino thanks the Funding from MINECO/FEDER (Project MAT2017-87579-R).

References

[1] N. Serpone and E. Pelizzetti, ed. in Photocatalysis: fundamentals and applications, Wiley Interscience, New York, 1st edn., 1989.

[2] J.M. Herrmann, Catal. Today 53 (1999) 115-129.

[3] A.L. Linsebigler, L. Guangquan, J.T. Yate, Photocatalysis on TiO_2 surfaces: Principles, mechanisms and selected results. Chem. Rev. 95 (1995) 735-758.

[4] M. Kaneko, I. Okura (2002). Photocatalysis: science and technology. Springer.

[5] C.M. Gómez, G. D. Angel, E. Ramos-Ramírez, I. Rangel-Vázquez, F. González, A. Arrieta, A. Vázquez-Zavala, A. Bonilla-Sánchez, M. Sánchez Cantú, J. Chem. Technol. Biotchnol. 91 (2016) 2211-2220.

[6] O.A. Zelekew, H.D. Kuo, J.M. Yassin, K.E. Ahmed, H. Abdullah, Appl. Surf. Sci. 410 (2017) 454-463.

[7] G. Zu, J. Shen, W. Wang, L. Zou, Y. Lian, Z. Zhang, Appl. Mater. Interfaces 7 (2015) 5400–5409.

[8] J. Matos, J. Laine, J.M. Herrmann. Appl. Catal. B. Environ. 18 (1998) 281-291.

[9] B. Tryba, A. Morawski, M. Inagaki. Appl. Catal. B. Environ. 41 (2003) 427-433.

[10] R. Leary, A. Westwood. Carbon 49 (2011) 741-772.

[11] Y. Hendrix, A. Lazaro, Q. Yu, Y. Brouwers. World J. Nano Science & Eng. 5 (2015) 161-177.

[12] C. Anderson, J. Barda. J. Phys. Chem. B. 101(1997) 2611-2616.

[13] Y Xu, W. Zheng, W. Liu. J. Photochem. PhotoBiol. A. Chem. 122 (1999) 57-60.

[14] HS. Kibombo, R Peng, S Rasalingam, RT. Koodali. Catal. Sci. Technol. 2 (2012) 1737-1766.

[15] M. Ahmaruzzaman, V.K. Gupta, Ind. Eng. Chem. Research, 50 (2011) 13589-13613.

[16] A.A. Alshatwi, J. Athinarayanan, V.S. Periasamy, Mater. Sci. Eng. C. Mater. Biol. Appl. 47 (2015) 8-16.

[17] Y. Shen, J. Agric. Food Chem. 65 (2017) 995-1004.

[18] F. Adam, J.N. Appaturi, A. Iqbal, Catal. Today 190 (2012) 2-14.

[19] J. Matos, A. García, S.E. Park, Appl. Catal. A: Gen. 393 (2011) 359-366.

[20] G. Mishra, K.M. Parida, S. K. Singh, RSC Advances, 25 (2014) 12918-12928.

[21] N.O. Mchedlov-Petrossyan, N.A. Vodolazkaya, A.O. Doroshenko, J. Fluorescence 13 (2003) 235-248.

[22] B.X. Wei, L. Zhao, T.J. Wang, H. Gao, H.X. Wu, Y. Jin, Adv. Powder Technol. 24 (2013) 708-713.

[23] R.J. Carmona, L.F. Velasco, M.C. Hidalgo, J.A. Navio, C.O. Ania, Appl. Catal A. 505 (2015) 467-477.

[24] T. Wu, G. Liu, J. Zhao, H. Hidaka, N. Serpone, J. Phys. Chem. B. 102 (1998) 5845-5851.

[25] O. Merka, V. Yarovyi, D.W. Bahnemann, M. Wark, J. Phys. Chem. C. 115 (2011) 8014-8023.

[26] H. Liu, M. Ren, Z. Zhang, J. Qu, Y. Ma, N. Lu, Environ. Sci. Pollut. Res. 25 (2018) 12361-12372.

[27] F. Rouquerol, J. Rouquerol, K.S.W. Sing, P. Llewellyn, G. Maurin, Adsorption by Powders and Porous Solids: Principles, Methodology and Applications, second ed., Elsevier, Oxford, 2014.

[28] J. Matos, S. Miralles-Cuevas, A. Ruíz-Delgado, I. Oller, S. Malato, Carbon 122 (2017) 361-373.

[29] B. Focher, P.L. Beltrame, A. Naggi, G. Torri, Carbohydr. Polym. 12 (1990) 405–418.

[30] L. Liang, P.C. Rieke, J. Liu, G.E. Fryxell, J.S. Young, M.H. Engelhard, K.L. Alford, Langmuir 16 (2000) 8016-8023.

[31] D. Rodríguez-Padrón, M. Algarra, L.A.C. Tarelho, J. Frade, A. Franco, G. de Miguel, J. Jiménez, E. Rodríguez-Castellón, R. Luque, ACS Sustainable Chem. Eng. 6 (2018) 7200–720.

[32] M.M. Titirici, A. Thomas, M. Antonietti, Adv. Functional Mater. 17 (2007) 1010-1018.

[33] A. Dasgupta, J. Matos, H. Muramatsu, Y. Ono, V. Gonzalez, H. Liu, C. Rotella, K. Fujisawa, R. Cruz-Silva, Y. Hashimoto, M. Endo, K. Kaneko, L.R. Radovic, M. Terrones, Carbon 139 (2018) 833-844.

[34] M.A. Hartley, J.N. Chiang, D.W. Hess, D.S. Soane, Appl. Phys. Lett. 54 (1989) 1510-1512.

[35] P. Yang, D. Zhao, D.I. Margolese, B.F. Chmelka, G.D. Stucky, Nature 396 (1998) 152-155.

[36] N. Reis, A.S. Franca, L.S. Oliveira, LWT-Food Sci. Technol. 50 (2013) 715-722.

[37] I.G. Markovska, L.A. Lyubchev, J. Therm. Anal. Cal. 89 (2007) 809-814.

[38] G. Sócrates. Infrared Characteristic Group Frequencies. John Wiley & Sons, New York, 1994, pp. 126-127.

[39] A.E. Ahmed, F. Adam, Micropor. Mesopor. Mater. 103 (2007) 284–295.

[40] H. Xiuli, X. Leqin, J. Xiaoxia, Z. Weiliang, J. Wuhan Univ. Technol. Mater. Sci. Ed. 32 (2017) 67-75.

[41] M.K. Gangishetty, K.E. Lee, R.W. Scott, T.L. Kelly, ACS Appl. Mater. Interfaces 5 (2013) 11044–11051.

[42] J.M. Ball, S.D. Stranks, M.T. Hörantner, S. Hüttner, W. Zhang, E.J.W. Crossland, E. Al, Energy Environ. Science 8 (2015) 602–609.

[43] L. Gracia, A. Beltran, D. Errandonea, Phys. Rev. B 80 (2009) 094105.

[44] F. Chen, J. Zhao, H. Hidaka, Inter. J. Photoenergy 05 (2003) 209-217.

[45] X. Chen, B. Chen, Environ. Sci. Technol. 49 (2015) 6181–6189.

[46] T. Cordero, C. Duchamp, J.M. Chovelon, C. Ferronato, J. Matos, J. Photochem. Photobiol. A: Chem. 191 (2007) 122-131.

[47] H. Fu, C. Pan, W. Yao, Y. Zhu. J. Phys. Chem. B. 109 (2005) 22432-22439.

[48] S. Murcia-López, M.C. Hidalgo, J.A. Navío, Appl. Catal. A: Gen. 466 (2013) 51–59.

[49] T. Saison, P. Gras, N. Chemin, C. Chaneac, O. Durupthy, V. Brezova, C. Colbeau-Justin, J.P. Jolivet. New insights into Bi_2WO_6 properties as a visible-light photocatalyst. J. Phys. Chem. C. 117 (2013) 22656−22666.

[50] H. Huang, Y. He, X. Li, M. Li, C. Zeng, F. Dong, X. Du, T. Zhang, Y. Zhang, J. Mater. Chem. A. 3 (2015) 24547-24556.

[51] H. Huang, X. Li, J. Wang, F. Dong, P.K. Chu, T. Zhang, Y. Zhang, ACS Catalysis 5 (2015) 4094-4103.

[52] H. Huang, S. Tu, C. Zeng, T. Zhang, A.H. Reshak, Y. Zhang, Angew. Chem. Int. Ed. 56 (2017) 11860-11864.

[53] H. Huang, A.H. Reshak, S. Auluck, S. Jin, N. Tian, Y. Guo, Y. Zhang, J. Phys. Chem. C. 122 (2018) 2661-2672.

[54] A. Phuruangrat, A. Maneechote, P. Dumrongrojthanath, N. Ekthammathat, S. Thongtem, T. Thongtem. Superlattices and Microstructures 78 (2015) 106–115

Table Captions

Table 1. Summary of atomic concentration (at. %) of the elements detected by XPS analysis.

Table 2. Selected textural, chemical and structural properties of the studied catalysts.

Table 3. Adsorption parameters for RhB obtained from fitting the experimental equilibrium adsorption data to the Langmuir and Freundlich model.

Table 4. Kinetic parameters for the RhB photodegradation.

Figure Captions

Figure 1. SEM images of the raw rice husk precursor at various magnifications.

Figure 2. SEM images of the prepared catalysts. (a-b): RH-Si; (c-d): RH-Si-350; (e-f): RH-Si-Ti; (g-h): RH-Si-Ti-350.

Figure 3. SEM-EDX analysis of sample RH-Si-Ti-350. (a-e): SEM images; (b-f): SEM images showing the analyzed regions; (c-d, g-h): EDX spectra.

Figure 4. C 1*s* core level spectra for the synthesized catalysts: (a): RH-Si; (b): RH-Si-350; (c): RH-Si-Ti; (d): RH-Si-Ti-350.

Figure 5. O 1*s* core level spectra of the synthesized catalysts: (a): RH-Si; (b): RH-Si-350; (c): RH-Si-Ti; (d): RH-Si-Ti-350.

Figure 6. Characterization of the prepared catalysts: (a) N_2 adsorption-desorption isotherms at -196 ºC; (b) FTIR spectra; (c) XRD patterns; (d) light absorption features.

Figure 7. Adsorption isotherms of RhB on the synthesized SiO_2-based catalysts. Symbols account for experimental data; dashed lines to the fitting with the Freundlich model.

Figure 8. RhB photocatalytic degradation in (a) SiO_2-based and (b): Ti-containing photocatalysts. Data corresponding to the photolytic reaction and the performance of commercial SiO_2 and TiO_2 catalysts is also included for comparison.

Figure 9. Changes in the absorbance of the UV-visible spectra of the solution as a function of the reaction time for the different biogenic SiO2-based photocatalysts.